Journal of Advanced Ceramics
2023, **12**(7): 1430–1440
https://doi.org/10.26599/JAC.2023.9220765
ISSN 2226-4108
CN 10-1154/TQ

Research Article

High-entropy rare-earth diborodicarbide: A novel class of high-entropy $(Y_{0.25}Yb_{0.25}Dy_{0.25}Er_{0.25})B_2C_2$ ceramics

Huidong Xu[a,b], Longfei Jiang[a], Ke Chen[a,b], Qing Huang[a,b], Xiaobing Zhou[a,b,*]

[a]*Engineering Laboratory of Advanced Energy Materials, Ningbo Institute of Materials Technology and Engineering, Chinese Academy of Sciences, Ningbo 315201, China*
[b]*University of Chinese Academy of Sciences, Beijing 100049, China*

Received: April 28, 2023; Revised: May 10, 2023; Accepted: May 10, 2023

Abstract: A novel class of high-entropy rare-earth metal diborodicarbide $(Y_{0.25}Yb_{0.25}Dy_{0.25}Er_{0.25})B_2C_2$ (HE-REB_2C_2) ceramics was successfully fabricated using the *in-situ* reactive spark plasma sintering (SPS) technology for the first time. Single solid solution with a typical tetragonal structure was formed, having a homogeneous distribution of four rare-earth elements, such as Y, Yb, Dy, and Er. Coefficients of thermal expansion (CTEs) along the *a* and *c* directions (α_a and α_c) were determined to be 4.18 and 16.06 μK^{-1}, respectively. Thermal expansion anisotropy of the as-obtained HE-REB_2C_2 was attributed to anisotropy of the crystal structure of HE-REB_2C_2. The thermal conductivity (k) of HE-REB_2C_2 was 9.2±0.09 $W \cdot m^{-1} \cdot K^{-1}$, which was lower than that of YB_2C_2 (19.2±0.07 $W \cdot m^{-1} \cdot K^{-1}$), DyB_2C_2 (11.9±0.06 $W \cdot m^{-1} \cdot K^{-1}$), and ErB_2C_2 (12.1±0.03 $W \cdot m^{-1} \cdot K^{-1}$), due to high-entropy effect and sluggish diffusion effect of high-entropy ceramics (HECs). Furthermore, Vickers hardness of HE-REB_2C_2 was slightly higher than that of REB_2C_2 owing to the solid solution hardening mechanism of HECs. Typical nano-laminated fracture morphologies, such as kink boundaries, delamination, and slipping were observed at the tip of Vickers indents, suggesting ductile behavior of HE-REB_2C_2. This newly investigated class of ductile HE-REB_2C_2 ceramics expanded the family of HECs to diboridcarbide compounds, which can lead to more research works on high-entropy rare-earth diboridcarbides in the near future.

Keywords: high-entropy rare-earth diboridcarbide; $(Y_{0.25}Yb_{0.25}Dy_{0.25}Er_{0.25})B_2C_2$ (REB_2C_2); high-entropy ceramics (HECs); thermal property; damage tolerance

1 Introduction

Ultra-high-temperature ceramics (UHTCs) have high melting points, outstanding oxidation resistance, along with excellent mechanical properties [1–4]. They have attracted increasing attention for aerospace applications, such as leading edges and a nose cone of hypersonic vehicles, as well as surface coatings for SiC-based ceramic matrix composites [5–10]. Since the service temperatures (T) of UHTCs are usually above 1800 ℃, most of UHTCs belong to highly covalent bonded ceramics, such as transition metal borides and carbides [11,12]. On the other hand, intrinsic brittleness and poor machinability of the transition metal borides and carbides obviously inhibited their applications as

* Corresponding author.
E-mail: zhouxb@nimte.ac.cn

ultra-high-temperature structure materials [13].

Rare-earth diborodicarbides (REB_2C_2, RE = Sc, Y, and lanthanide elements), which were first developed by Post *et al*. [14] in 1956, are a new group of ternary layered structure materials, similar to MAX phases (where M is an early transition metal, A is the IIIA, IVA, VA, or VIA group elements, and X is carbon (C) or nitrogen) [15]. YB_2C_2 is a typical compound of the REB_2C_2 family, which has been widely investigated [16–19]. The crystal structure of YB_2C_2 was reported as the tetragon with two types of a space group of $P4_2/mmc$ (No. 131) and $P4/mbm$ (No. 127) [20,21]. In YB_2C_2, Y and B_2C_2 layers are alternatively stacking along the *c* direction. In the Y layers, Y–Y bonds are metallic bonds, while boron (B)–C bonds are covalent bonds in the B_2C_2 layers. The Y and B_2C_2 layers are mainly bonded by van der Waals force. Particularly, in the B_2C_2 layers, B and C atoms form four-member and eight-member B–C rings. The theoretical calculation results indicated that YB_2C_2 presents strong anisotropy in elastic properties owing to anisotropy of chemical bonds [19].

Furthermore, YB_2C_2 was reported as machinable layered ceramics with fracture toughness of 4.6±0.1 $MPa{\cdot}m^{1/2}$ and excellent damage tolerance. The residual flexural strength under Vickers contact load of 200 N was reported to be 80% [22]. Very recently, Li *et al*. [17] demonstrated that YB_2C_2 is stable at such a high temperature as 2500 ℃ for 20 min, which suggested that the melting point of YB_2C_2 is in the temperature range of 2500–2550 ℃. Therefore, YB_2C_2 has been considered as a promising candidate for ultra-high-temperature applications.

On the other hand, high-entropy ceramics (HECs) are solid solution of inorganic compounds with one or more Wyckoff sites shared by equal or near equal atomic ratios of multi-principal elements [23]. HECs have drawn considerable attention due to their four core effects similar to high-entropy alloys (HEAs), i.e., (i) high-entropy effect: Configuration entropies in HEAs are much higher than those of conventional alloys, reducing free energy of a solid solution phase and promoting the formation of the solid solution [24]. (ii) Severe lattice distortion: The difference in the atomic size causes a lattice distortion, resulting in solid solution strengthening and hardening [25]. (iii) Sluggish diffusion effect inhibits the grain growth of a second phase [26]. (iv) Cocktail effect results in unexpected properties due to the solid solution formed by several elements [27]. Compared to HEAs, HECs have larger space for improvement of the properties expanding through band structure and phonon engineering [23]. In contrast to conventional ceramics, HECs have been reported to possess excellent mechanical properties, such as superior-hardness, lower thermal conductivity (k), good thermodynamic stability, and improved corrosion and oxidation resistance [28–31]. Therefore, the high-entropy concept is a novel strategy for UHTCs due to low thermal conductivity and excellent thermal stability of such materials [28,32]. On the other hand, the hardness of the HECs is usually higher than their counterparts for traditional HE borides and carbides, resulting in solid solution strengthening and hardening mechanism. Therefore, the development of a ductile and damage tolerant HE ceramic for ultra-high-temperature applications is an interesting research topic.

Recently, the expansion of the HEC family has been relatively fast. A large number of papers on high-entropy carbides, borides, oxides, and silicides have been reported [33–36]. However, to the best of the authors' knowledge, there has been no report on the development of high-entropy rare-earth diboridecarbides.

Therefore, the aim of this work was to expand the family of HECs. A new class of ductile nature and damage tolerance high-entropy rare-earth diborodicarbide with the composition of $(Y_{0.25}Yb_{0.25}Dy_{0.25}Er_{0.25})B_2C_2$ (REB_2C_2) was successfully synthesized using *in-situ* reactive spark plasma sintering (SPS) for the first time. Microstructures, coefficients of thermal expansion (CTEs) in the *a* and *c* directions (α_a and α_c), thermal conductivity, and Vickers hardness of the as-obtained high-entropy $(Y_{0.25}Yb_{0.25}Dy_{0.25}Er_{0.25})B_2C_2$ (HE-REB_2C_2) were investigated.

2 Experimental procedure

2.1 Starting materials

REH_2 (RE = Y, Yb, Dy, and Er) powders with purity of 99.9% and a mean particle size of ~75 μm were purchased from Hunan Rare Earth Metal Materials Reasearch Insititute Co., Ltd., Changsha, China. B_4C powders with purity of 99% and a mean particle size of ~14 μm were purchased from Mudanjiang Diamond Boron Carbide Co., Ltd., Mudanjiang, China. The mean particle size of carbon black (99.9%, EnoMaterial Co., Ltd., Qinhuangdao, China) was ~20 nm. REH_2, B_4C, and C powders were used as starting materials.

2. 2 *In-situ* reactive SPS process

To fabricate the HE-REB_2C_2 ceramics, REH_2, B_4C, and C powders were mixed in a stoichiometric ratio of 2 : 1 : 3, where the molar ratio of YH_2 : YbH_2 : DyH_2 : ErH_2 in REH_2 was 1 : 1 : 1 : 1. The *in-situ* reactive SPS process was performed in an SPS furnace (HPD-25, FCT Systeme GmbH, Germany) in an Ar atmosphere at a target temperature of 1800 ℃ for 15 min under a uniaxial pressure of 30 MPa. To promote the *in-situ* reaction, a pre-reaction at 1600 ℃ for 30 min was set before the target sintering temperature of 1800 ℃. The heating and cooling rates were both 50 ℃·min^{-1}. For the sake of comparison, the monolithic YB_2C_2, YbB_2C_2, DyB_2C_2, and ErB_2C_2 ceramics were prepared using the same sintering conditions.

2. 3 Material characterization

Phase compositions and crystal structures of the samples were identified by an X-ray diffractometer (D8 Advance, Bruker AXS, Germany) equipped with Cu Kα radiation (λ = 1.5406 Å) under operating power of 1600 W (a current of 40 mA and a voltage of 40 kV) at a step scan of 2θ = 0.02° and step time of 0.2 s. The phase compositions and the lattice parameters of the as-synthesized HE-REB_2C_2 were determined by Rietveld refinement of the XRD patterns using the TOPAS-Academic v6 software. Furthermore, α_a and α_c of the as-obtained HE-REB_2C_2 were measured using a high-temperature X-ray diffractometer (D8 Advance, Bruker AXS, Germany) in vacuum at a step scan of 2θ = 0.02° and step time of 0.2 s at the temperature range of 300–773 K. The heating rate was 50 ℃·min^{-1} for 10 min. Expanded lattice parameters were determined by Rietveld analysis of high-temperature X-ray diffraction (XRD) patterns using the TOPAS-Academic v6 software.

Microstructures and chemical compositions of the samples were detected by a scanning electron microscope (SEM; Regulus 8230, Hitachi, Japan) equipped with an energy-dispersive spectroscopy (EDS) system. The mean grain sizes (d) of the samples were determined using several selected SEM images, where at least 100 grains were measured. Thin foils of the samples for transmission electron microscopy (TEM) observations were prepared using the focused ion beam (FIB) technique (Aurgia, Carl Zeiss, USA). Aberration-correction TEM images of HE-REB_2C_2 were observed by a double spherical aberration-correction transmission electron microscope (Spectra 300, ThermoFisher, USA).

The apparent density (ρ) of the samples was measured by Archimedes' method. The specific heat capacity (c_p) and thermal diffusivity coefficient (α) were determined by the laser flash method using a Netzsch equipment (LFA467, NETZSCH- Gerätebau GmbH, Germany) in an argon atmosphere at 323 K. The k (W·m^{-1}·K^{-1}) is calculated by Eq. (1):

$$k = \rho\alpha c_p \tag{1}$$

Vickers hardness of the as-obtained samples was measured by a Vickers hardness tester (Wilson VH3300, Buehler, USA) under loads of 5, 10, 20, and 30 N. The dwell time at the maximum load was 15 s.

3 Results and discussion

3. 1 Microstructure of as-obtained HE-REB_2C_2

Figures 1(a)–1(e) show SEM images of the fractured surfaces of REB_2C_2 (RE = Y, Yb, Dy, and Er) and HE-REB_2C_2 samples. A typical nano-laminated structure, similar to MAX phases, was observed for the samples of both REB_2C_2 (RE = Y, Yb, Dy, and Er) and HE-REB_2C_2 samples. The main fracture mechanism observed in all samples was intergranular fracture along with pull-out of the plate-like laminated grains. The laminated fracture, such as kink band, delamination, and slipping, was observed, which suggested ductile nature of both REB_2C_2 (RE = Y, Yb, Dy, and Er) and HE-REB_2C_2 samples. The d of REB_2C_2 (RE = Y, Yb, Dy, and Er) and HE-REB_2C_2, including length and thickness, is shown in Fig. 2. Both the length and the thickness of the HE-REB_2C_2 grains were finer than those of single REB_2C_2 ceramics (RE = Y, Yb, Dy, and Er), due to sluggish diffusion effect of HECs [37]. On the other hand, few pores were observed on the fracture surfaces of all samples, except the sample YbB_2C_2, which showed increased porosity. This was in good agreement with density and open porosity results (Table 1).

Figure 3(a) shows XRD patterns of the REB_2C_2 (RE = Y, Yb, Dy, and Er) and HE-REB_2C_2 samples sintered at 1800 ℃. The REB_2C_2 phase was the predominant phase in all samples, while some RE–B (including REB_4 and REB_6), RE–O, and RE–B–O impurities were detected. According to Rietveld refinement results, the amounts of the main YB_2C_2, YbB_2C_2, DyB_2C_2, and ErB_2C_2 phases were 72.91, 60.36, 75.21, and 72.81 wt%, respectively. At the same time, the XRD pattern

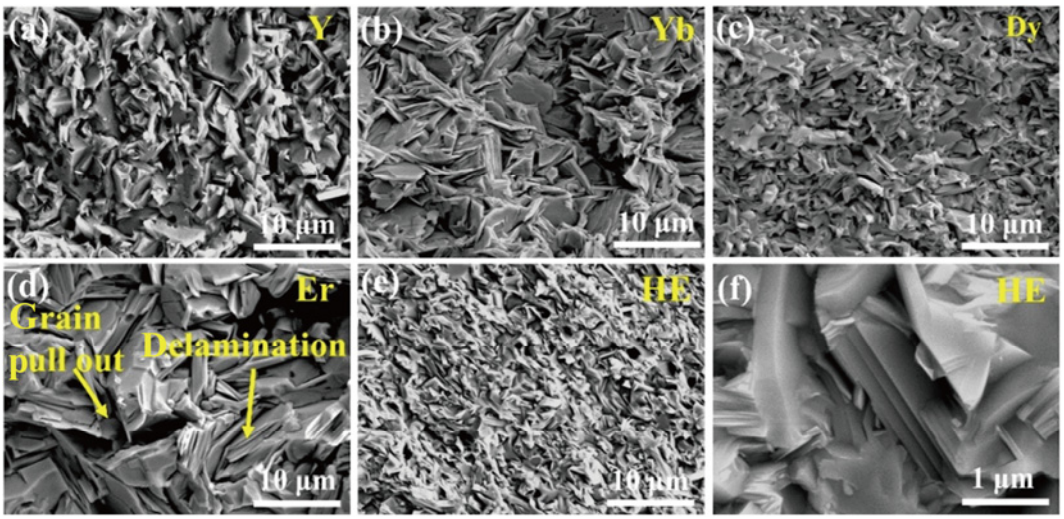

Fig. 1 (a–e) Low- and (f) high-magnification SEM images of fracture surfaces of REB_2C_2 (RE = Y, Yb, Dy, and Er) and HE-REB_2C_2 sintered at 1800 ℃.

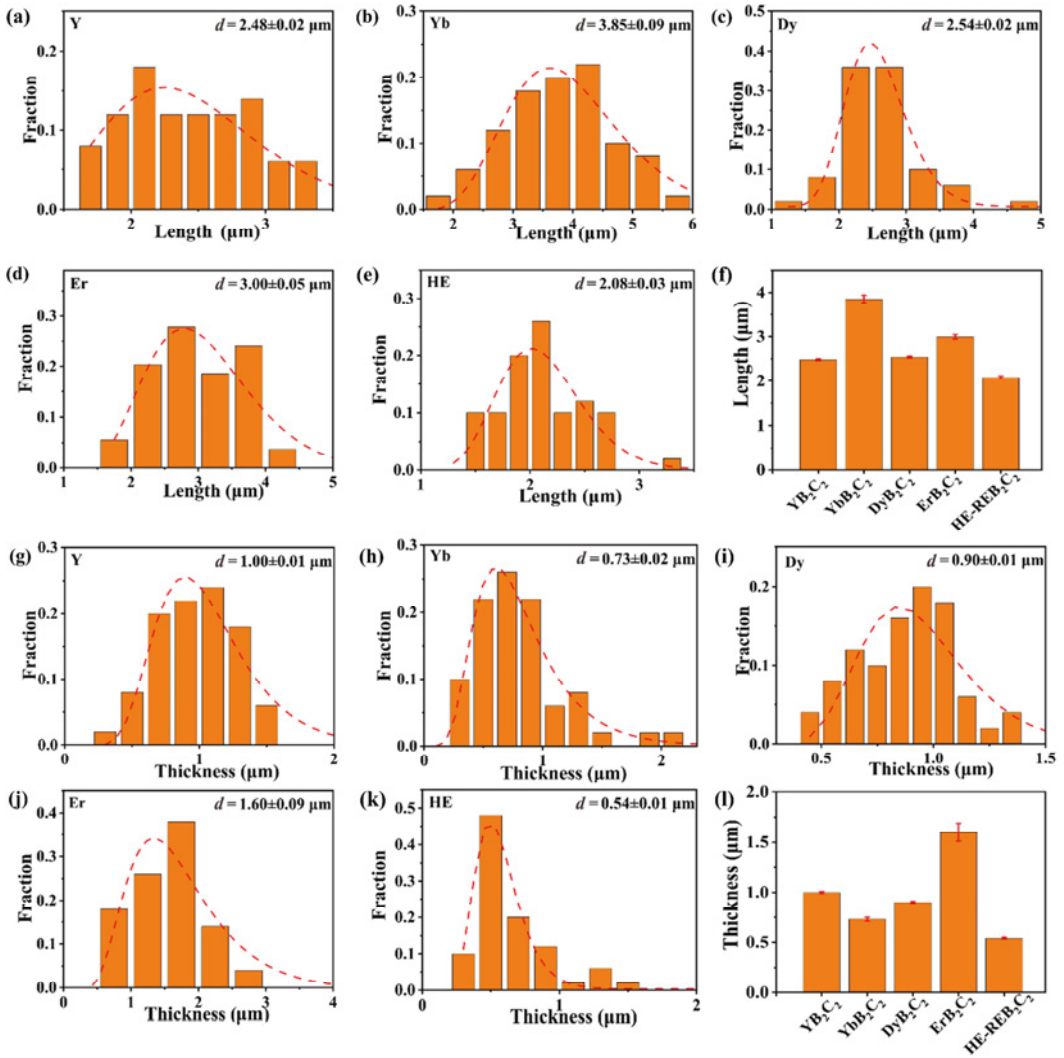

Fig. 2 (a–e) Grain lengths of REB_2C_2 (RE = Y, Yb, Dy, or Er) and HE-REB_2C_2, (f) comparison of grain lengths of REB_2C_2 (RE = Y, Yb, Dy, and Er) and HE-REB_2C_2, (g–k) grain thicknesses of REB_2C_2 (RE = Y, Yb, Dy, and Er) and HE-REB_2C_2, and (l) comparison of grain thicknesses of REB_2C_2 (RE = Y, Yb, Dy, and Er) and HE-REB_2C_2.

Table 1 Open porosity, density, relative density, and grain sizes of high-entropy $(Y_{0.25}Yb_{0.25}Dy_{0.25}Er_{0.25})B_2C_2$ and REB_2C_2 (RE = Y, Yb, Dy, and Er) samples

Compound	Open porosity (%)	Density (g/cm^3)		Relative density (%)	Grain size (μm)	
		Experimental	Calculated		Length	Thickness
HE-REB_2C_2	0.27	6.12	6.31	97.0	2.08±0.03	0.54±0.01
YB_2C_2	0.17	4.05	4.12	98.3	2.48±0.02	1.00±0.01
YbB_2C_2	1.38	6.56	7.14	91.9	3.85±0.09	0.73±0.02
DyB_2C_2	0.19	6.34	6.49	97.7	2.54±0.02	0.90±0.01
ErB_2C_2	0.13	6.73	6.76	99.6	3.00±0.05	1.60±0.09

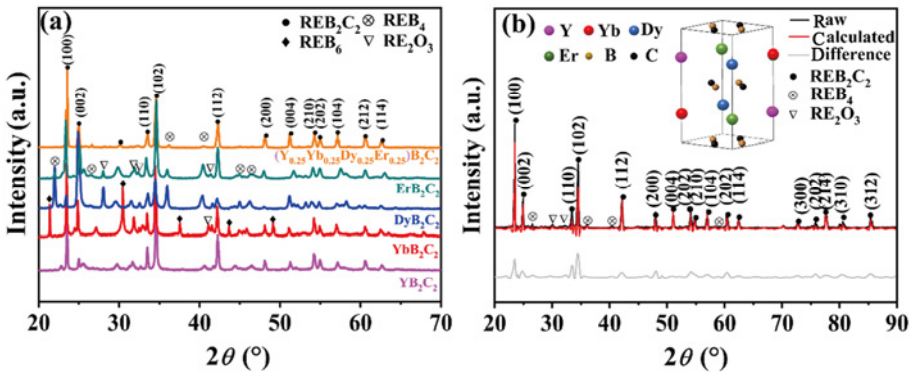

Fig. 3 (a) XRD pattern of as-synthesized $(Y_{0.25}Yb_{0.25}Dy_{0.25}Er_{0.25})B_2C_2$ and corresponding XRD patterns of YB_2C_2, YbB_2C_2, DyB_2C_2, and ErB_2C_2 and (b) Rietveld refinement of XRD pattern of as-synthesized $(Y_{0.25}Yb_{0.25}Dy_{0.25}Er_{0.25})B_2C_2$.

of the HE-REB_2C_2 sample was almost identical, which confirmed that both the HE-REB_2C_2 and the REB_2C_2 (RE = Y, Yb, Dy, and Er) materials consisted of the homologous crystal structure. Figure 3(b) presents the typical Rietveld refinement of the XRD pattern of HE-REB_2C_2. Rietveld fitting results (reliability factor (R_{wp}) = 9.863%) showed that a tetragonal structure was the predominant phase, which is a characteristic structure of the REB_2C_2 phase. The sample consisted of 88.63 wt% high-entropy $(Y_{0.25}Yb_{0.25}Dy_{0.25}Er_{0.25})B_2C_2$ phase with a small amount of REB_4 (8.22 wt%), and RE_2O_3 (3.15 wt%).

Refined lattice parameters (*a* and *c*) of the as-obtained HE-REB_2C_2 and REB_2C_2 (RE = Y, Yb, Dy, and Er) are given in Table 2. The *a* and *c* of the HE-REB_2C_2 phase were 3.78 and 7.14 Å, respectively, which were close to the mean values of the corresponding four reference compositions REB_2C_2 (RE = Y, Yb, Dy, and Er). It is interesting to note that the lattice distortion of HE-REB_2C_2 occurred mainly along the *c* direction, while no significant change was observed for the lattice parameters in the *a* direction when compared to those of the single-composition REB_2C_2. This can be explained based on the crystal structure of REB_2C_2. In the inner of the B_2C_2 layers and RE layers, there are strong chemical bonds between the atoms in the *a* direction, such as B–C covalent bonds and RE–RE metallic bonds. On the other hand, relatively weak van der Waals forces exist between the B_2C_2 layers and the RE layers along the *c* direction [19]. Therefore, the lattice distortion of the HE-REB_2C_2 structure was favorable in the *c* direction.

Table 2 *a* and *c* of high-entropy $(Y_{0.25}Yb_{0.25}Dy_{0.25}Er_{0.25})B_2C_2$ and the reference REB_2C_2 (RE = Y, Yb, Dy, and Er) samples

Compound	Experimental		Theoretical		Reference card
	a (Å)	*c* (Å)	*a* (Å)	*c* (Å)	
HE-REB_2C_2	3.78	7.14	—	—	This study
YB_2C_2	3.78	7.12	3.79	7.12	PDF#27-0971
YbB_2C_2	3.78	7.13	3.78	7.40	ICSD#612680
DyB_2C_2	3.78	7.13	3.78	7.12	PDF#26-0586
ErB_2C_2	3.78	7.02	3.79	7.09	ICSD#612593

The possible formation process of HE-REB_2C_2 is similar to the formation mechanism of REB_2C_2 [22]. First, REH_2 decomposed to RE and release H_2. The RE and C diffused to the surface of B_4C to form HE-REB_2C_2. The main reactions can be summarized as Reactions (2)–(4):

$$REH_2 \rightarrow RE + H_2 \quad (2)$$

$$2RE + B_4C + 3C \rightarrow 2REB_2C_2 \quad (3)$$

$$2(Y_{0.25} + Yb_{0.25} + Dy_{0.25} + Er_{0.25}) + B_4C + 3C \rightarrow 2(Y_{0.25}Yb_{0.25}Dy_{0.25}Er_{0.25})B_2C_2 \quad (4)$$

Figure 4 shows an SEM image of the polished surface of the high-entropy $(Y_{0.25}Yb_{0.25}Dy_{0.25}Er_{0.25})B_2C_2$ ceramics and the corresponding rare-earth elemental distributions of Y, Yb, Dy, and Er. The EDS mappings indicated that the four rare-earth elements of Y, Yb, Dy, and Er were homogeneously distributed in the selected area at the micrometer scale, confirming chemical homogeneity of the HE-REB_2C_2 sample. Furthermore, the semi-quantitative EDS analysis results of the spots 1–3 are given in Table 3. The results showed that the atomic ratios of the rare-earth elements (Y, Yb, Dy, and Er) are approximately equal, which indicated that the multiple rare-earth elements had similar solid solubility in the as-obtained HE-REB_2C_2 ceramics.

To further confirm the microstructures and phase compositions of the HE-REB_2C_2 samples, the atomic-scale microstructure along the [001] zone axis was performed by high-resolution transmission electron microscopy (HR-TEM) and corresponding selected area electron diffraction (SAED) pattern, as shown in Fig. 5. It revealed that the as-synthesized HE-REB_2C_2 possessed a single crystal tetragonal structure as a result of the well-arranged diffraction spots with the symmetry. Figures 5(b) and 5(c) show the atomic-resolution high-angle annular dark field (HAADF) scanning transmission electron microscopy (STEM) image and annular bright field (ABF) STEM image of the HE-REB_2C_2 ceramics, respectively. The atomic-resolution HAADF and ABF images showed an atomic configuration of atoms in the view of the [001] zone axis. The lattice fringe spacing of 0.3956 nm were assigned to the (100) plane of HE-REB_2C_2. The HAADF image is related to the *z* contrast, which is proportional to the square of an atomic number [38]. The contrast of ABF image is proportional to 1/3 of an atomic number, so it is more sensitive to light elements than the HAADF image [39]. Therefore, it clearly showed the positions of the light atoms, such as B and C. The atomic configuration of the atoms (Figs. 5(b) and 5(c)) indicated that the planes of rare-earth atom and the planes of B–C atom planes are alternately stacked, which is consistent with the crystal structure of HE-REB_2C_2 detected by XRD.

3. 2 CTEs of HE-REB_2C_2

Thermal expansion behavior is a critical thermal property of the materials for ultra-high-temperature applications, which is caused by anharmonic vibration of atoms in a temperature field [40,41]. Therefore, the expansion of the lattice parameters of the as-obtained HE-REB_2C_2 was detected using high-temperature XRD at the temperature range of 303–773 K, as shown in Fig. 6. There was no phase decomposition and transformation in the measured temperature range, which implied that the HE-REB_2C_2 material was stable at the temperatures up to 773 K. The evolution of the (100) and (002) peaks with the increasing temperature indicates the thermal expansion of the HE-REB_2C_2 lattice along the *a* and *c* directions, respectively. It was clearly shown that no significant shift of the (100) peak was

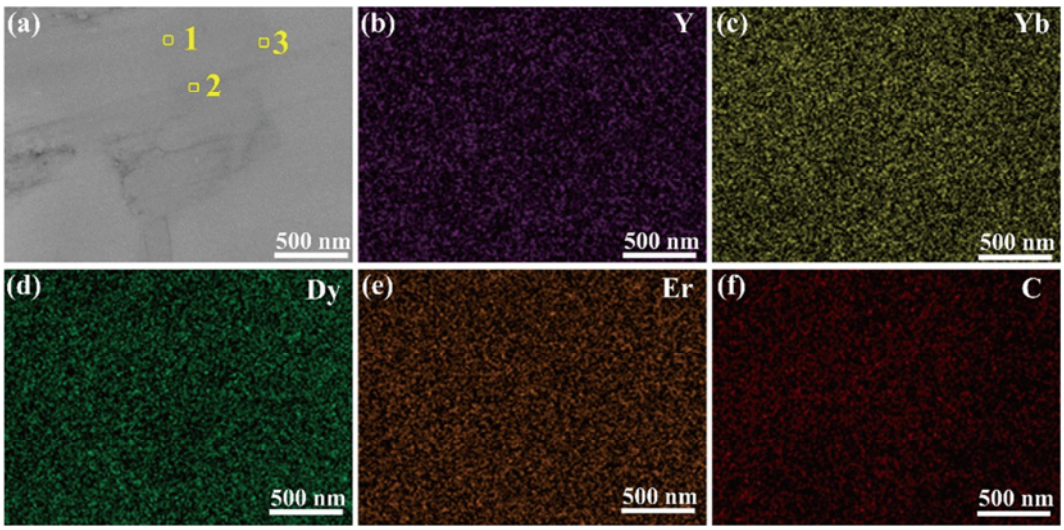

Fig. 4 (a) SEM image of polished surface of high-entropy $(Y_{0.25}Yb_{0.25}Dy_{0.25}Er_{0.25})B_2C_2$ ceramics and (b–f) corresponding EDS elemental mappings.

Table 3 EDS results of spots 1–3 in Fig. 4(a)

No.	Atomic composition (at%)			
	Y	Yb	Dy	Er
1	16.8	27.9	27.0	28.3
2	15.2	25.9	28.2	30.7
3	18.1	28.9	29.2	23.8

observed with the increase in the temperature (Fig. 6(b)), while the (002) peak was obviously shifted to the left with the increasing temperature. This clearly reveals the anisotropy of the thermal expansion of the HE-REB_2C_2 structure in the *a* and *c* directions. The expanded lattice parameters were calculated by Rietveld refinements using the TOPAS-Academic v6 software.

The α_a and α_c can be calculated by Eqs. (5) and (6), respectively [42]:

$$\alpha_a = \frac{\mathrm{d}(a(T))}{a_0 \mathrm{d}T} \tag{5}$$

$$\alpha_c = \frac{\mathrm{d}(c(T))}{c_0 \mathrm{d}T} \tag{6}$$

where $\frac{\mathrm{d}(a(T))}{\mathrm{d}T}$ and $\frac{\mathrm{d}(c(T))}{\mathrm{d}T}$ are the slopes of the fitted linear functions of $a(T)$ and $c(T)$, respectively, and a_0 and c_0 are the lattice parameters at room temperature (~303 K). Furthermore, the average CTE

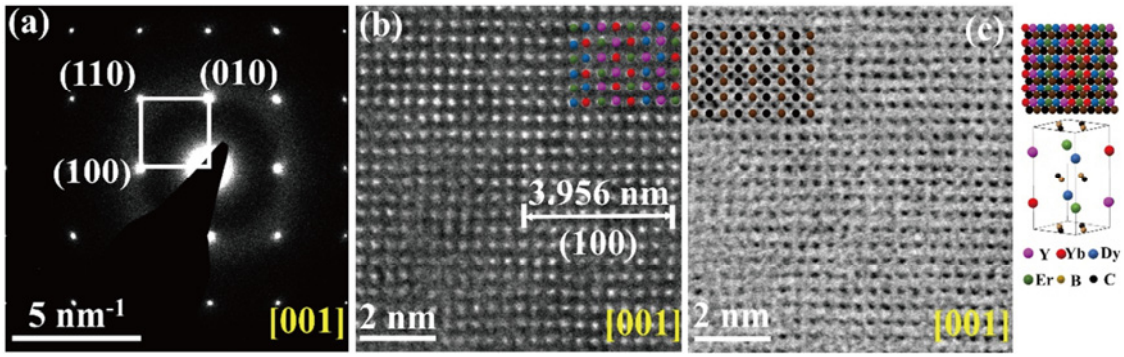

Fig. 5 (a) SAED pattern of HE-REB_2C_2 sample, (b) atomic-resolved HAADF image of HE-REB_2C_2 showing atomic arrangements along [001] direction, and (c) atomic-resolved ABF image of HE-REB_2C_2.

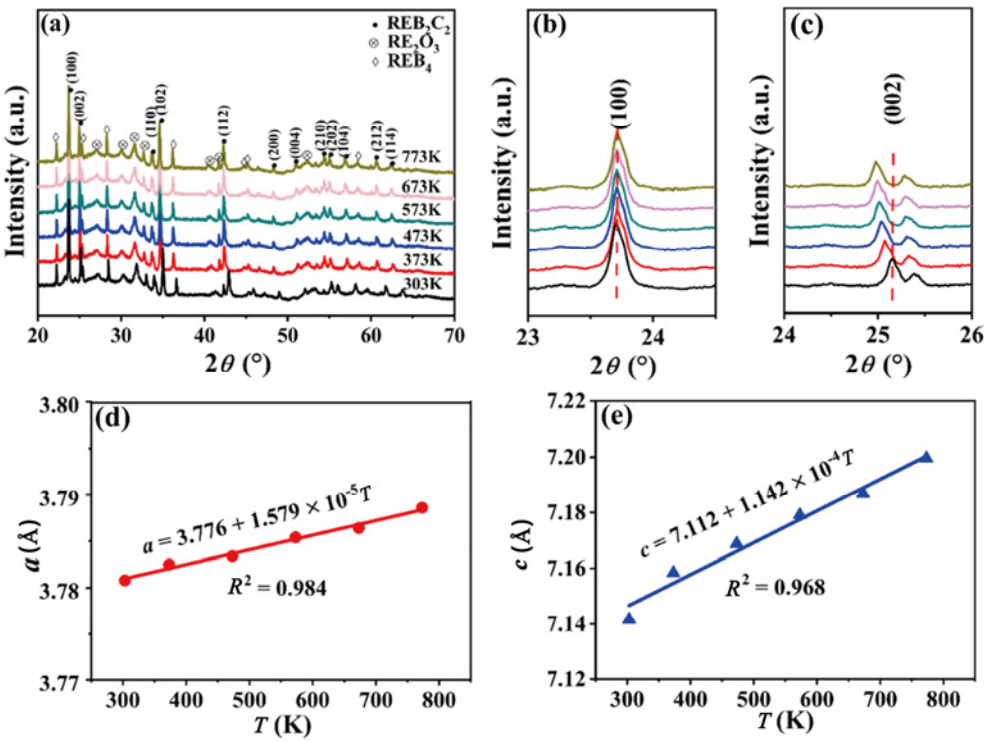

Fig. 6 (a) XRD patterns of high-entropy $(Y_{0.25}Yb_{0.25}Dy_{0.25}Er_{0.25})B_2C_2$ structure at different temperatures, (b, c) partial XRD patterns of high-entropy $(Y_{0.25}Yb_{0.25}Dy_{0.25}Er_{0.25})B_2C_2$ showing peak shift of (100) and (002) planes, respectively, and fitted lattice parameters of (d) *a* and (e) *c* as a function of *T* (R^2 reflects the fitness of the curve to experimental values).

(α_{av}) can be obtained by Eq. (7) [42]:

$$\alpha_{av} = \frac{2\alpha_a + \alpha_c}{3} \quad (7)$$

According to the calculated results of Eqs. (5)–(7), α_a, α_c, and α_{av} of the as-obtained HE-REB_2C_2 were 4.18, 16.06, and 8.14 μK^{-1}, respectively. This clearly confirmed that the HE-REB_2C_2 structure exhibits the thermal expansion anisotropy along the *a* and *c* directions. The α_c/α_a ratio is usually used to characterize the degree of the anisotropy of the thermal expansion. The ratio of α_c/α_a calculated for the HE-REB_2C_2 structure was 3.84. It should be noted that the value of α_c/α_a ratio of HE-REB_2C_2 is significantly greater than those of some typical MAX phases, such as Ti_3SiC_2 (1.09) [43], Ti_3AlC_2 (1.33) [44], and Ti_2AlC (1.41) [45]. This suggested the anisotropy in the thermal expansion of HE-REB_2C_2 is more significant when compared to the MAX phase. This phenomenon can be explained by the crystal structure of HE-REB_2C_2. In REB_2C_2, the RE and B_2C_2 layers are alternatively stacked along the *c* direction to form a layered structure [17]. The chemical bonds between the RE and B_2C_2 layers are RE–B and RE–C bonds along the *c* direction, which are weaker than the highly covalent B–C bonds in the B_2C_2 planes along the *a* direction. According to the calculated results of the YB_2C_2 structure, the length of B–C bonds within the four-member B–C rings is 1.6196 Å, while the lengths of C–C and B–B bonds that connect the eight-member B–C rings are 1.2755 and 1.7613 Å, respectively. On the other hand, the lengths of Y–C and Y–B bonds are 2.6789 and 2.7477 Å, respectively [19]. Such a significant difference in bond lengths (roughly inferring the bond energy) along the *a* and *c* directions resulted in the obvious anisotropic thermal properties of the HE-REB_2C_2 structure.

3.3 Thermal conductivity of HE-REB_2C_2 and REB_2C_2

Figure 7 shows thermal conductivity of the as-obtained HE-REB_2C_2 and REB_2C_2 (RE = Y, Yb, Dy, and Er) materials. It should be noted that, the lowest thermal conductivity was measured for the YbB_2C_2 sample, due to its highest porosity (lowest relative density), as shown in Table 1. Since the result was strongly affected by the porosity of the sample, this sample was not compared to the HE-REB_2C_2 material.

The thermal conductivity of the HE-REB_2C_2 sample was 9.2±0.09 $W \cdot m^{-1} \cdot K^{-1}$, which was lower than those of YB_2C_2 (19.2±0.07 $W \cdot m^{-1} \cdot K^{-1}$), DyB_2C_2 (11.9±0.06 $W \cdot m^{-1} \cdot K^{-1}$), and ErB_2C_2 (12.1±0.03 $W \cdot m^{-1} \cdot K^{-1}$). This can be attributed to the high-entropy effect. The presence of four rare-earth elements in the solid solution leads to lattice distortion, which improves phonon scattering and increases thermal resistance [46]. On the other hand, the impurities of RE–B and RE–O, which have higher thermal conductivity than that of HE-REB_2C_2 [47,48], also affect the thermal conductivity. Therefore, the higher purity of the high-entropy $(Y_{0.25}Yb_{0.25}Dy_{0.25}Er_{0.25})B_2C_2$ phase (88.63 wt%) resulted in lower thermal conductivity when compared to those of the reference single-composition REB_2C_2 (RE = Y, Dy, and Er). Furthermore, the grain sizes of the HE-REB_2C_2 material (both the length and the thickness of the grains) were lower than those of YB_2C_2, DyB_2C_2, and ErB_2C_2 due to the sluggish diffusion effect of HECs. The phonon scattering caused by grain boundaries increases as the grain size decreases. Therefore, the sample with the finest grain size (HE-REB_2C_2) contained the highest number of grain boundaries, at which the phonon scattering occurs, resulting in the lowest thermal conductivity among all of the investigated materials [49]. In addition, it should be noted that the electronic thermal conductivity of HE-REB_2C_2 was also changed when compared to those of the reference single-composition REB_2C_2 (RE = Y, Yb, Dy, and Er) due to the high-entropy effect. The contribution of the electric thermal conductivity of REB_2C_2 and HE-REB_2C_2 is unclear until now, and we will investigate it in the future work.

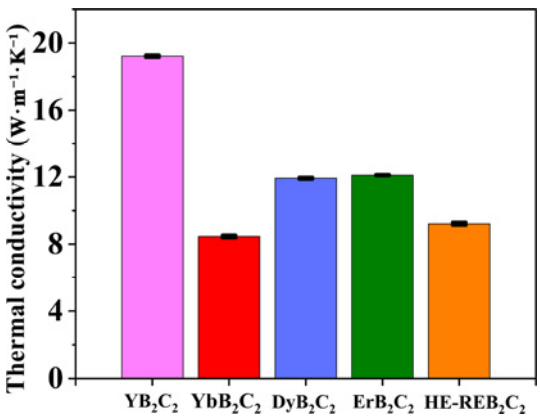

Fig. 7 Thermal conductivity of as-obtained HE-REB_2C_2 and REB_2C_2 (RE = Y, Yb, Dy, and Er) materials.

3.4 Vickers hardness of HE-REB_2C_2 and REB_2C_2

Figure 8(a) shows Vickers hardness as a function of the load for the as-obtained high-entropy $(Y_{0.25}Yb_{0.25}Dy_{0.25}Er_{0.25})B_2C_2$ and REB_2C_2 (RE = Y, Yb, Dy, and Er)

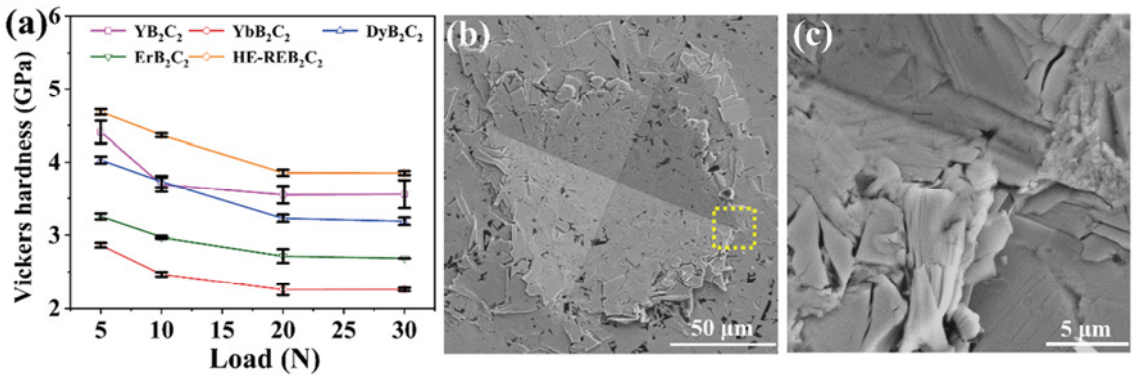

Fig. 8 (a) Vickers hardness of high-entropy $(Y_{0.25}Yb_{0.25}Dy_{0.25}Er_{0.25})B_2C_2$ and REB_2C_2 (RE = Y, Yb, Dy, and Er) materials as a function of load and (b, c) low- and high-magnification SEM images of HE-REB_2C_2 surface after Vickers indentation under load of 20 N, respectively.

materials as a function of load. The hardness of the HE-REB_2C_2 material gradually decreased from 4.68±0.04 to 3.85±0.03 GPa as the load increased from 5 to 30 N, respectively, due to indentation load size effect [50]. On the other hand, Vickers hardness of HE-REB_2C_2 samples was slightly higher than the hardness of the reference single-composition REB_2C_2 (RE = Y, Yb, Dy, and Er). For example, Vickers hardness of HE-REB_2C_2 and REB_2C_2 (RE = Y, Yb, Dy, and Er) measured under the load of 30 N were 3.85±0.03, 3.56±0.19, 2.26±0.02, 3.19±0.05, and 2.69±0.03 GPa, respectively. This can be attributed to the disorder among rare-earth species and the solid solution hardening mechanism [51]. The multi rare-earth element doping led to the increased configuration entropy and the intensified lattice distortion, which increased the resistance against dislocation movement. As a result, the hardness of HE-REB_2C_2 was improved [52]. It is interesting that the hardness of the HE- REB_2C_2 was just slightly higher than the hardness of the reference YB_2C_2. It can be ascribed to the fact that the weak chemical bonds between the RE and B_2C_2 layers along the *c* direction, which led to slipping and delamination preferentially preference along the basal plane, as shown in Figs. 8(b) and 8(c). As a result, the solid solution hardening effect was not so much obviously, as was reported in some typical high-entropy borides and carbides [53,54].

Figures 8(b) and 8(c) show low- and high-magnification SEM images of the HE-REB_2C_2 surface after Vickers indentation under a load of 20 N, respectively. No typically extended cracks propagating from corners of the indents, which are usually observed for brittle ceramics, were found in this study, suggesting ductile nature of HE-REB_2C_2 ceramics [55]. The morphology of Vickers indents was irregular with exfoliated surfaces and deformed particles, and was similar to the shapes of the indent in the MAX phases [56]. When the basal plane was parallel to the load, the laminated fracture was observed owing to the slipping, delamination, and kink formation. On the other hand, the exfoliation occurred when the basal plane was perpendicular to the applied load. The deformation during the indentation of HE-REB_2C_2 can be ascribed to the basal plane slipping and debonding at the interface between the RE and B_2C_2 layers [19].

4 Conclusions

In summary, the novel high-entropy rare-earth metal diborodicarbide $(Y_{0.25}Yb_{0.25}Dy_{0.25}Er_{0.25})B_2C_2$ was successfully fabricated using an *in-situ* solid state reaction via SPS. The as-obtained HE-REB_2C_2 showed the single solid solution with a typical tetragonal structure. The four rare-earth elements, such as Y, Yb, Dy, and Er, occupied the RE position in the REB_2C_2 structure, which was revealed by the atomic-resolved HAADF and ABF images of HE-REB_2C_2. The evolution of lattice parameters of HE-REB_2C_2 was determined by the high-temperature XRD, followed by Rietveld refinements. The thermal expansion anisotropy of HE-REB_2C_2 along the *a* and *c* directions was observed. The value of α_c/α_a was 3.84, confirming the significant anisotropy of the HE-REB_2C_2 structure. Compared to the reference REB_2C_2 compositions (RE = Y, Dy, and Er), HE-REB_2C_2 exhibited lower thermal conductivity (9.2±0.09 $W \cdot m^{-1} \cdot K^{-1}$) due to the high-entropy effect and sluggish diffusion effect. In addition, Vickers hardness of the HE-REB_2C_2 material was 3.85±0.03 GPa, which was just slightly higher than that of the reference YB_2C_2. The investigated

novel ductile nature of the HE-REB_2C_2 ceramics paved the way for the applications as the new class of UHTCs in the aerospace area.

Acknowledgements

This study was supported by the National Natural Science Foundation of China (Grant Nos. 12275337 and 11975296) and the Natural Science Foundation of Ningbo City (Grant No. 2021J199). We would like to recognize the support from the Ningbo 3315 Innovative Teams Program, China (Grant No. 2019A-14-C). Thanks for the financial support of Advanced Energy Science and Technology Guangdong Laboratory (Grant No. HND20TDTHGC00).

Declaration of competing interest

The authors have no competing interests to declare that are relevant to the content of this article.

References

[1] Lun HL, Zeng Y, Xiong X, *et al*. Oxidation behavior of non-stoichiometric (Zr,Hf,Ti)C_x carbide solid solution powders in air. *J Adv Ceram* 2021, **10**: 741–757.

[2] Peters AB, Wang CH, Zhang DJ, *et al*. Reactive laser synthesis of ultra-high-temperature ceramics HfC, ZrC, TiC, HfN, ZrN, and TiN for additive manufacturing. *Ceram Int* 2023, **49**: 11204–11229.

[3] Li F, Huang X, Liu JX, *et al*. Sol–gel derived porous ultra-high temperature ceramics. *J Adv Ceram* 2020, **9**: 1–16.

[4] Nisar A, Zhang C, Boesl B, *et al*. Synthesis of $Hf_6Ta_2O_{17}$ superstructure via spark plasma sintering for improved oxidation resistance of multi-component ultra-high temperature ceramics. *Ceram Int* 2023, **49**: 783–791.

[5] Zhang Y, Sun SK, Guo WM, *et al*. Optimal preparation of high-entropy boride–silicon carbide ceramics. *J Adv Ceram* 2021, **10**: 173–180.

[6] Zheng YP, Zou MC, Zhang WY, *et al*. Electrical and thermal transport behaviours of high-entropy perovskite thermoelectric oxides. *J Adv Ceram* 2021, **10**: 377–384.

[7] Naik AK, Nazeer M, Prasad DKVD, *et al*. Development of functionally graded ZrB_2–B_4C composites for lightweight ultrahigh-temperature aerospace applications. *Ceram Int* 2022, **48**: 33332–33339.

[8] Wang KW, Ma BS, Li T, *et al*. Fabrication of high-entropy perovskite oxide by reactive flash sintering. *Ceram Int* 2020, **46**: 18358–18361.

[9] Yan SX, Luo SH, Yang L, *et al*. Novel P2-type layered medium-entropy ceramics oxide as cathode material for sodium-ion batteries. *J Adv Ceram* 2022, **11**: 158–171.

[10] Rubio V, Ramanujam P, Cousinet S, *et al*. Thermal properties and performance of carbon fiber-based ultra-high temperature ceramic matrix composites (C_f-UHTCMCs). *J Am Ceram Soc* 2020, **103**: 3788–3796.

[11] Zhang WM, Zhao B, Xiang HM, *et al*. One-step synthesis and electromagnetic absorption properties of high entropy rare earth hexaborides (HE REB_6) and high entropy rare earth hexaborides/borates (HE REB_6/HE $REBO_3$) composite powders. *J Adv Ceram* 2021, **10**: 62–77.

[12] Yu L, Liu H, Fu YH, *et al*. Design and preparation of an ultra-high temperature ceramic by *in-situ* introduction of $Zr_2[Al(Si)]_4C_5$ into ZrB_2–SiC: Investigation on the mechanical properties and oxidation behavior. *J Adv Ceram* 2021, **10**: 1082–1094.

[13] Golla BR, Mukhopadhyay A, Basu B, *et al*. Review on ultra-high temperature boride ceramics. *Prog Mater Sci* 2020, **111**: 100651.

[14] Post B, Moskowitz D, Glaser FW. Borides of rare earth metals. *J Am Chem Soc* 1956, **78**: 1800–1802.

[15] Zhou AG, Liu Y, Li SB, *et al*. From structural ceramics to 2D materials with multi-applications: A review on the development from MAX phases to MXenes. *J Adv Ceram* 2021, **10**: 1194–1242.

[16] Nguyen VQ, Kim JS, Lee SH. Synthesis of YB_2C_2 by high-energy ball milling and reactive spark plasma sintering. *J Am Ceram Soc* 2021, **104**: 1229–1236.

[17] Li YM, Tian L, Bao YW, *et al*. YB_2C_2: The first damage tolerant ceramic with melting point over 2500 ℃. *J Eur Ceram Soc* 2023, **43**: 3830–3835.

[18] Yang Y, Hong T. Mechanical and thermodynamic properties of YB_2C_2 under pressure. *Physica B* 2017, **525**: 154–158.

[19] Zhou YC, Xiang HM, Wang XH, *et al*. Electronic structure and mechanical properties of layered compound YB_2C_2: A promising precursor for making two dimensional (2D) B_2C_2 nets. *J Mater Sci Technol* 2017, **33**: 1044–1054.

[20] Reckeweg O, DiSalvo FJ. Different structural models of YB_2C_2 and GdB_2C_2 on the basis of single-crystal X-ray data. *Z Naturforsch B* 2014, **69**: 289–293.

[21] Khmelevskyi S, Mohn P, Redinger J, *et al*. Electronic structure of the layered diboride dicarbide superconductor YB_2C_2. *Supercond Sci Tech* 2005, **18**: 422–426.

[22] Zhao GR, Chen JX, Li YM, *et al*. YB_2C_2: A machinable layered ternary ceramic with excellent damage tolerance. *Scripta Mater*2016, **124**: 86–89.

[23] Xiang HM, Xing Y, Dai FZ, *et al*. High-entropy ceramics: Present status, challenges, and a look forward. *J Adv Ceram* 2021, **10**: 385–441.

[24] Nie SY, Wu L, Zhao LC, *et al*. Entropy-driven chemistry reveals highly stable denary $MgAl_2O_4$-type catalysts. *Chem Catal* 2021, **1**: 648–662.

[25] Rost CM, Rak Z, Brenner DW, *et al*. Local structure of the $Mg_xNi_xCo_xCu_xZn_xO$ (x = 0.2) entropy-stabilized oxide: An EXAFS study. *J Am Ceram Soc* 2017, **100**: 2732–2738.

[26] Ye BL, Wen TQ, Nguyen MC, *et al*. First-principles study, fabrication and characterization of $(Zr_{0.25}Nb_{0.25}Ti_{0.25}V_{0.25})C$ high-entropy ceramics. *Acta Mater* 2019, **170**: 15–23.

[27] Ishizu N, Kitagawa J. New high-entropy alloy superconductor $Hf_{21}Nb_{25}Ti_{15}V_{15}Zr_{24}$. *Results Phys* 2019, **13**: 102275.

[28] Chen H, Xiang HM, Dai FZ, *et al*. High porosity and low thermal conductivity high entropy $(Zr_{0.2}Hf_{0.2}Ti_{0.2}Nb_{0.2}Ta_{0.2})C$. *J Mater Sci Technol* 2019, **35**: 1700–1705.

[29] Zhang PX, Ye L, Chen FH, *et al*. Stability, mechanical, and thermodynamic behaviors of (TiZrHfTaM)C (M = Nb, Mo, W, V, Cr) high-entropy carbide ceramics. *J Alloys Compd* 2022, **903**: 163868.

[30] Wang X, Cheng MH, Xiao GZ, *et al*. Preparation and corrosion resistance of high-entropy disilicate $(Y_{0.25}Yb_{0.25}Er_{0.25}Sc_{0.25})_2Si_2O_7$ ceramics. *Corros Sci* 2021, **192**: 109786.

[31] Guo WJ, Hu J, Ye YC, *et al*. Ablation behavior of (TiZrHfNbTa)C high-entropy ceramics with the addition of SiC secondary under an oxyacetylene flame. *Ceram Int* 2022, **48**: 12790–12799.

[32] Chen H, Xiang HM, Dai FZ, *et al*. Porous high entropy $(Zr_{0.2}Hf_{0.2}Ti_{0.2}Nb_{0.2}Ta_{0.2})B_2$: A novel strategy towards making ultrahigh temperature ceramics thermal insulating. *J Mater Sci Technol* 2019, **35**: 2404–2408.

[33] Dong Y, Ren K, Wang QK, *et al*. Interaction of multicomponent disilicate $(Yb_{0.2}Y_{0.2}Lu_{0.2}Sc_{0.2}Gd_{0.2})_2Si_2O_7$ with molten calcia–magnesia–aluminosilicate. *J Adv Ceram* 2022, **11**: 66–74.

[34] Zhang WM, Xiang HM, Dai FZ, *et al*. Achieving ultra-broadband electromagnetic wave absorption in high-entropy transition metal carbides (HE TMCs). *J Adv Ceram* 2022, **11**: 545–555.

[35] Gild J, Samiee M, Braun JL, *et al*. High-entropy fluorite oxides. *J Eur Ceram Soc* 2018, **38**: 3578–3584.

[36] Gild J, Braun J, Kaufmann K, *et al*. A high-entropy silicide: $(Mo_{0.2}Nb_{0.2}Ta_{0.2}Ti_{0.2}W_{0.2})Si_2$. *J Materiomics* 2019, **5**: 337–343.

[37] Zhu JT, Wei MY, Xu J, *et al*. Influence of order–disorder transition on the mechanical and thermophysical properties of $A_2B_2O_7$ high-entropy ceramics. *J Adv Ceram* 2022, **11**: 1222–1234.

[38] Bao WC, Wang XG, Ding HJ, *et al*. High-entropy M_2AlC–MC (M = Ti, Zr, Hf, Nb, Ta) composite: Synthesis and microstructures. *Scripta Mater*2020, **183**: 33–38.

[39] Findlay SD, Shibata N, Sawada H, *et al*. Dynamics of annular bright field imaging in scanning transmission electron microscopy. *Ultramicroscopy* 2010, **110**: 903–923.

[40] Wang XD, Chen K, Wu EX, *et al*. Synthesis and thermal expansion of chalcogenide MAX phase Hf_2SeC. *J Eur Ceram Soc* 2022, **42**: 2084–2088.

[41] Wang XD, Chen K, Li ZQ, *et al*. MAX phases $Hf_2(Se_xS_{1-x})C$ (x = 0–1) and their thermal expansion behaviors. *J Eur Ceram Soc* 2023, **43**: 1874–1879.

[42] Miller W, Smith CW, Mackenzie DS, *et al*. Negative thermal expansion: A review. *J Mater Sci* 2009, **44**: 5441–5451.

[43] Manoun B, Saxena SK, Liermann HP, *et al*. Thermal expansion of polycrystalline Ti_3SiC_2 in the 25–1400 ℃ temperature range. *J Am Ceram Soc* 2005, **88**: 3489–3491.

[44] Scabarozi TH, Amini S, Leaffer O, *et al*. Thermal expansion of select $M_{n+1}AX_n$ (M = early transition metal, A =A group element, X = C or N) phases measured by high temperature X-ray diffraction and dilatometry. *J Appl Phys* 2009, **105**: 013543.

[45] Barsoum MW, El-Raghy T, Ali M. Processing and characterization of Ti_2AlC, Ti_2AlN, and $Ti_2AlC_{0.5}N_{0.5}$. *Metall Mater Trans A* 2000, **31**: 1857–1865.

[46] Zhu JT, Meng XY, Zhang P, *et al*. Dual-phase rare-earth-zirconate high-entropy ceramics with glass-like thermal conductivity. *J Eur Ceram Soc* 2021, **41**: 2861–2869.

[47] Klein PH, Croft WJ. Thermal conductivity, diffusivity, and expansion of Y_2O_3, $Y_3Al_5O_{12}$, and LaF_3 in the range 77–300 K. *J Appl Phys* 1967, **38**: 1603–1607.

[48] Peters R, Kränkel C, Fredrich-Thornton ST, *et al*. Thermal analysis and efficient high power continuous-wave and mode-locked thin disk laser operation of Yb-doped sesquioxides. *Appl Phys B* 2011, **102**: 509–514.

[49] Ahmad K, Almutairi Z, Almuzaiqer R, *et al*. Processing and thermal properties of $SrTiO_3/Ti_3AlC_2$ ceramic nanocomposites. *Ceram Int* 2022, **48**: 18739–18744.

[50] Kathavate VS, Kumar BP, Singh I, *et al*. Analysis of indentation size effect (ISE) in nanoindentation hardness in polycrystalline PMN–PT piezoceramics with different domain configurations. *Ceram Int* 2021, **47**: 11870–11877.

[51] Senkov ON, Senkova SV, Woodward C, *et al*. Low-density, refractory multi-principal element alloys of the Cr–Nb–Ti–V–Zr system: Microstructure and phase analysis. *Acta Mater* 2013, **61**: 1545–1557.

[52] Castle E, Csanádi T, Grasso S, *et al*. Processing and properties of high-entropy ultra-high temperature carbides. *Sci Rep* 2018, **8**: 8609.

[53] Zhang Y, Guo WM, Jiang ZB, *et al*. Dense high-entropy boride ceramics with ultra-high hardness. *Scripta Mater*2019, **164**: 135–139.

[54] Harrington TJ, Gild J, Sarker P, *et al*. Phase stability and mechanical properties of novel high entropy transition metal carbides. *Acta Mater* 2019, **166**: 271–280.

[55] Shi LK, Zhou XB, Dai JQ, *et al*. Microstructure and properties of nano-laminated $Y_3Si_2C_2$ ceramics fabricated via *in situ* reaction by spark plasma sintering. *J Adv Ceram* 2021, **10**: 578–586.

[56] Zhou XB, Jing L, Kwon YD, *et al*. Fabrication of SiC_w/Ti_3SiC_2 composites with improved thermal conductivity and mechanical properties using spark plasma sintering. *J Adv Ceram* 2020, **9**: 462–470.